

# The Heavy Photon Search Test Detector

M. Battaglieri<sup>a</sup>, S. Boyarinov<sup>b</sup>, S. Bueltmann<sup>c</sup>, V. Burkert<sup>b</sup>, A. Celentano<sup>a</sup>, G. Charles<sup>f</sup>, W. Cooper<sup>d</sup>, C. Cuevas<sup>b</sup>, N. Dashyan<sup>e</sup>, R. DeVita<sup>a</sup>, C. Desnault<sup>f</sup>, A. Deur<sup>b</sup>, H. Egriyan<sup>b</sup>, L. Elouadrhiri<sup>b</sup>, R. Essig<sup>g</sup>, V. Fadeyev<sup>h</sup>, C. Field<sup>i</sup>, A. Freyberger<sup>b</sup>, Y. Gershtein<sup>j</sup>, N. Gevorgyan<sup>e</sup>, F.-X. Girod<sup>b</sup>, N. Graf<sup>i</sup>, M. Graham<sup>i</sup>, K. Griffioen<sup>k</sup>, A. Grillo<sup>h</sup>, M. Guidal<sup>f</sup>, G. Haller<sup>i</sup>, P. Hansson Adrian<sup>i,\*</sup>, R. Herbst<sup>i</sup>, M. Holtrop<sup>l</sup>, J. Jaros<sup>i</sup>, S. Kaneta<sup>b</sup>, M. Khandaker<sup>m</sup>, A. Kubarovsky<sup>n</sup>, V. Kubarovsky<sup>b</sup>, T. Maruyama<sup>i</sup>, J. McCormick<sup>i</sup>, K. Moffeit<sup>i</sup>, O. Moreno<sup>h</sup>, H. Neal<sup>i</sup>, T. Nelson<sup>i</sup>, S. Niccolai<sup>f</sup>, A. Odian<sup>i</sup>, M. Oriunno<sup>i</sup>, R. Paremuzyan<sup>e</sup>, R. Partridge<sup>i</sup>, S. K. Phillips<sup>l</sup>, E. Rauly<sup>f</sup>, B. Raydo<sup>b</sup>, J. Reichert<sup>j</sup>, E. Rindfuss<sup>f</sup>, P. Rosier<sup>f</sup>, C. Salgado<sup>m</sup>, P. Schuster<sup>o</sup>, Y. Sharabian<sup>b</sup>, D. Sokhan<sup>p</sup>, S. Stepanyan<sup>b</sup>, N. Toro<sup>o</sup>, S. Uemura<sup>i</sup>, M. Ungaro<sup>b</sup>, H. Voskanyan<sup>e</sup>, D. Walz<sup>i</sup>, L. B. Weinstein<sup>c</sup>, B. Wojtsekhowski<sup>b</sup>

<sup>a</sup>Istituto Nazionale di Fisica Nucleare, Sezione di Genova e Dipartimento di Fisica dell'Università, 16146 Genova, Italy

<sup>b</sup>Thomas Jefferson National Accelerator Facility, Newport News, Virginia 23606

<sup>c</sup>Old Dominion University, Norfolk, Virginia 23529

<sup>d</sup>Fermi National Accelerator Laboratory, Batavia, IL 60510-5011

<sup>e</sup>Yerevan Physics Institute, 375036 Yerevan, Armenia

<sup>f</sup>Institut de Physique Nucléaire, CNRS/IN2P3 and Université Paris Sud, Orsay, France

<sup>g</sup>Stony Brook University, Stony Brook, NY 11794-3800

<sup>h</sup>Santa Cruz Institute for Particle Physics, University of California, Santa Cruz, CA 95064

<sup>i</sup>SLAC National Accelerator Laboratory, Menlo Park, CA 94025

<sup>j</sup>Rutgers University, Department of Physics and Astronomy, Piscataway, NJ 08854

<sup>k</sup>The College of William and Mary, Department of Physics, Williamsburg, VA 23185

<sup>l</sup>University of New Hampshire, Department of Physics, Durham, NH 03824

<sup>m</sup>Norfolk State University, Norfolk, Virginia 23504

<sup>n</sup>Rensselaer Polytechnic Institute, Department of Physics, Troy, NY 12181

<sup>o</sup>Perimeter Institute, Ontario, Canada N2L 2Y5

<sup>p</sup>University of Glasgow, Glasgow, G12 8QQ, Scotland, UK

---

## Abstract

The Heavy Photon Search (HPS), an experiment to search for a hidden sector photon in fixed target electroproduction, is preparing for installation at the Thomas Jefferson National Accelerator Facility (JLab) in the Fall of 2014. As the first stage of this project, the HPS Test Run apparatus was constructed and operated in 2012 to demonstrate the experiment's technical feasibility and to confirm that the trigger rates and occupancies are as expected. This paper describes the HPS Test Run apparatus and readout electronics and its performance. In this setting, a heavy photon can be identified as a narrow peak in the  $e^+e^-$  invariant mass spectrum above the trident background or as a narrow invariant mass peak with a decay vertex displaced from the production target, so charged particle tracking and vertexing are needed for its detection. In the HPS Test Run, charged particles are measured with a compact forward silicon microstrip tracker inside a dipole magnet. Electromagnetic showers are detected in a PbWO<sub>4</sub> crystal calorimeter situated behind the magnet, and are used to trigger the experiment and identify electrons and positrons. Both detectors are placed close to the beam line and split top-bottom. This arrangement provides sensitivity to low-mass heavy photons, allow clear passage of the unscattered beam, and avoids the spray of degraded electrons coming from the target. The discrimination between prompt and displaced  $e^+e^-$  pairs requires the first layer of silicon sensors be placed only 10 cm downstream of the target. The expected signal is small, and the trident background huge, so the experiment requires very large statistics. Accordingly, the HPS Test Run utilizes high-rate readout and data acquisition electronics and a fast trigger to exploit the essentially 100% duty cycle of the CEBAF accelerator at JLab.

**Keywords:** silicon, microstrip, tracking, vertexing, heavy photon, dark photon, electromagnetic calorimeter

---

1    **1. Introduction**

2    The heavy photon ( $A'$ ), aka a “hidden sector” or  
3    “dark” photon, is a massive gauge boson which couples  
4    weakly to electric charge by mixing with the Standard  
5    Model photon [1, 2]. Consequently, it can be radiated  
6    by electrons and subsequently decay into  $e^+e^-$  pairs, al-  
7   beit at rates far below those of QED trident processes.  
8    Heavy photons have been suggested by numerous be-  
9   yond Standard Model theories [3] to explain the discrep-  
10   ancy between theory and experiment of the muon’s  $g-2$   
11   [4], and as a possible explanation of recent astrophysical  
12   anomalies, e.g. [5, 6, 7]. Heavy photons couple directly  
13   to hidden sector particles with “dark” or “hidden sec-  
14   tor” charge; these particles could constitute all or some  
15   of the dark matter, e.g. [8, 9]. Current phenomenology  
16   highlights the  $20 - 1000 \text{ MeV}/c^2$  mass range, and sug-  
17   gests that the coupling to electric charge,  $\epsilon e$ , has  $\epsilon$  in the  
18   range of  $10^{-3} - 10^{-5}$ . This range of parameters makes  
19    $A'$  searches viable in medium energy fixed target elec-  
20   troproduction [10], but requires large data sets and good  
21   mass resolution to identify a small mass peak above the  
22   copious QED background. At small couplings, the  $A'$   
23   becomes long-lived, so detection of a displaced decay  
24   vertex can reject the prompt QED background and boost  
25   experimental sensitivity.

26    The HPS experiment [11] is preparing for installation  
27   in Hall-B at JLab in the Fall of 2014 to search for heavy  
28   photons by directing the 2.2-6.6 GeV CEBAF12 elec-  
29   tron beam onto a thin ( $0.25\% X_0$ ) Tungsten target foil.  
30    The HPS experiment uses both invariant mass and sec-  
31   ondary vertex signatures to search for  $A'$  decays into  
32    $e^+e^-$  pairs. At CEBAF energies, the  $A'$  decay products  
33   are boosted along the beam axis with small opening an-  
34   gles. For couplings  $\epsilon \ll 10^{-3}$ ,  $A'$  decay lengths range  
35   from millimeters to tens of centimeters and beyond. Ac-  
36   cordingly the tracking detectors cover opening angles  
37   down to 15 mrad and are placed just 10 cm downstream  
38   of the target.

39    HPS employs a 90 cm long silicon tracking and  
40   vertexing detector located inside a dipole magnet to  
41   measure momenta and decay vertex positions. A fast  
42   PbWO<sub>4</sub> electromagnetic calorimeter downstream of the  
43   magnet provides the trigger and electron identification.  
44    Both the silicon tracker and the ECal have  $\sim$ ns tim-  
45   ing resolution, which eliminates much of the out-of-  
46   time background from multiple scattered beam elec-  
47   trons. Fast front end electronics and high trigger and

48    data rate capability and the effectively 100% duty cycle  
49   of the CEBAF accelerator allows HPS to accumulate the  
50   very large statistics needed to be sensitive to the highly  
51   suppressed production of heavy photons.

52    The HPS Test Run, using a simplified version of the  
53   HPS apparatus, was proposed and approved at JLab as  
54   the first stage of HPS. Its purposes included demonstra-  
55   ting that the apparatus and data acquisition systems are  
56   technically feasible and the trigger rates and occupan-  
57   cies to be encountered in electron-beam running are as  
58   simulated. Given dedicated running time with electron  
59   beams, the HPS Test Run apparatus is capable of search-  
60   ing for heavy photons in unexplored regions of param-  
61   eter space. Therefore, key design criteria and require-  
62   ments for HPS and the HPS Test Run apparatus are the  
63   same:

- 64   • uniform acceptance between 15 and approximately  
65   70 mrad in the forward region to catch boosted de-  
66   cay products close to the beam,
- 67   • beam passage through the apparatus in vacuum, to  
68   eliminate direct interactions with the detector and  
69   minimize beam gas interactions,
- 70   • detector components that can survive and effi-  
71   ciently operate in a high radiation environment  
72   with some localized doses at the 100 Mrad level,
- 73   • high-rate electronics, handling trigger rates up to  
74   50 kHz and data rates of 100 MB/s to permanent  
75   storage,
- 76   • a flexible, redundant and efficient trigger for select-  
77   ing electron and positron pairs, capable of handling  
78   rates up to 50 kHz,
- 79   • hit reconstruction efficiency higher than 99% and  
80   average track reconstruction efficiency higher than  
81   98% for electrons and positrons,
- 82   • 2 ns hit time resolution in the silicon vertex tracker,
- 83   •  $A'$  mass resolution of 2.5% or better, which trans-  
84   lates to momentum resolution of 4.5% and angular  
85   resolution of 2 mrad/ $p(\text{GeV}/c)$  for  $B=0.5 \text{ T}$ ,
- 86   • resolution of distance of closest approach to the  
87   beam axis less than 250 (100)  $\mu\text{m}$  for tracks with  
88   0.5 (1.7)  $\text{GeV}/c$ . This gives a decay length resolu-  
89   tion of about 1 mm for a 100  $\text{MeV}/c^2 A'$ .
- 90   • PbWO<sub>4</sub> electromagnetic calorimeter energy reso-  
91   lution  $\Delta E/E \leq 5\%/\sqrt{E}$  and transverse segmentation  
92    $\sim 1.5 \text{ cm}$  (< Moliere radius in PbWO<sub>4</sub>). The en-  
93   ergy resolution requirement for triggering is less

---

\*Corresponding author.

Email address: phansson@slac.stanford.edu (P. Hansson Adrian)

94 stringent because the electrons and positrons have  
95  $E > 0.5$  GeV. The segmentation provides good  
96 spatial resolution and guarantees minimal shower  
97 overlap with background hits.

98 The HPS Test Run apparatus was installed on April  
99 19, 2012, and ran parasitically in the photon beam of  
100 the HDice experiment [12] until May 18. The JLab run  
101 schedule precluded any dedicated electron beam run-  
102 ning, but the HPS Test Run was allowed an eight hour  
103 dedicated photon beam run at the end of scheduled CE-  
104 BAF running. During this dedicated period,  $e^+e^-$  pairs,  
105 produced in a gold foil upstream of the experiment,  
106 were studied. With no dedicated electron beam run-  
107 ning, it was not possible to search for an  $A'$ . However,  
108 the final running provided enough data to demonstrate  
109 the functionality of the apparatus, document its perfor-  
110 mance, and explore trigger rates, as shown below.

111 This paper reviews the HPS Test Run apparatus, doc-  
112 umenting the performance of the trigger, data acquisi-  
113 tion, silicon tracking and vertex detector, and the elec-  
114 tromagnetic calorimeter at, or close to, the level re-  
115 quired for the HPS experiment.

## 116 2. Detector Overview

117 The HPS Test Run apparatus was designed to run in  
118 Hall B at JLab using the CEBAF 499 MHz electron  
119 beam at energies between 2.2 and 6.6 GeV and cur-  
120 rents between 200 and 600 nA. The overall design of  
121 the experiment follows from the kinematics of  $A'$  pro-  
122 duction which typically results in a final state particle  
123 within a few degrees of the incoming beam, especially  
124 at low  $m_{A'}$ . Detectors must therefore be placed close  
125 to the beam. The intense electron beam enlarges down-  
126 stream after multiple scattering in the target and elec-  
127 trons which have radiated in the target disperse horizon-  
128 tally in the field of the analyzing magnet. Together they  
129 constitute a “wall of flame” which must be completely  
130 avoided. Accordingly, the apparatus is split vertically  
131 to avoid a “dead zone”, the region within  $\pm 15$  mrad of  
132 the beam plane. In addition, the beam is transported in  
133 vacuum through the tracker to minimize beam-gas inter-  
134 action backgrounds. Even with these precautions, the  
135 occupancies of sensors near the beam plane are high,  
136 dominated by the multiple Coulomb scattering of the  
137 primary beam, so high-rate detectors, a fast trigger, and  
138 excellent time tagging are required to minimize their  
139 impact. The trigger comes from a highly-segmented  
140 lead-tungstate ( $PbWO_4$ ) crystal calorimeter located just  
141 downstream of the dipole magnet.

143 A rendering of the apparatus installed on the beam line  
144 is shown in Figure 1 and an overview of the coverage,  
145 segmentation and performance is given in Table 1.

146 The silicon tracking and vertexing detector for the  
147 HPS Test Run, or SVT, resides in a vacuum cham-  
148 ber inside the Pair Spectrometer (PS) dipole magnet in  
149 Hall B at JLab. The magnetic field strength was 0.5 T  
150 oriented vertically throughout the run. The SVT has  
151 five measurement stations, or “layers,” beginning 10 cm  
152 downstream of the target. Each layer comprises a pair  
153 of closely-spaced silicon microstrip sensors responsi-  
154 ble for measuring a single coordinate, or “view”. In-  
155 troduction of a small (50 or 100 mrad) stereo angle  
156 between the two sensors of each layer provides three-  
157 dimensional tracking and vertexing throughout the ac-  
158 ceptance of the detector. In order to accommodate the  
159 dead zone, the SVT is built in two halves that are ap-  
160 proximately mirror reflections of one another about the  
161 plane of the nominal electron beam. Each layer in one  
162 half is supported on a common support plate with inde-  
163 pendent cooling and readout.

164 The electromagnetic calorimeter (ECal) is also split  
165 into two halves. Each half of the ECal consists of  
166 221  $PbWO_4$  crystals arranged in rectangular formation.  
167 There are five rows with 46 crystals in each row except  
168 the row closest to the beam plane which has 37. The  
169 light from each crystal is read out by an Avalanche Photo-  
170 diode (APD) glued on the back surface of the crys-  
171 tal. Signals from the APDs are amplified using custom-  
172 made amplifier boards before being sent to the data ac-  
173 quisition electronics.

174 The Data Acquisition system combines two architec-  
175 tures, the Advanced Telecom Communications Archi-  
176 tecture (ATCA) based SVT readout system and VME-  
177 bus Switched Serial (VXS) based digitization and trig-  
178 gering system for the ECal.

## 179 3. The HPS Test Run Beamline

180 Since an electron beam was unavailable, the HPS Test  
181 Run detected the electrons and positrons produced by  
182 interactions of the secondary photon beam with a thin  
183 foil just upstream of the detectors. The HPS Test Run  
184 studied the performance of the detectors and the mul-  
185 tiple Coulomb scattering of the electrons and positrons.  
186 Figure 2 shows the layout of the setup on the beam line.  
187 The SVT was installed inside the Hall B pair spectrom-  
188 eter magnet vacuum chamber with the ECal mounted  
189 downstream of it. Both the SVT and the ECal were re-  
190 tracted off the beam plane compared to nominal electron  
191 beam running to allow clean passage of the photon beam  
192 through the system.

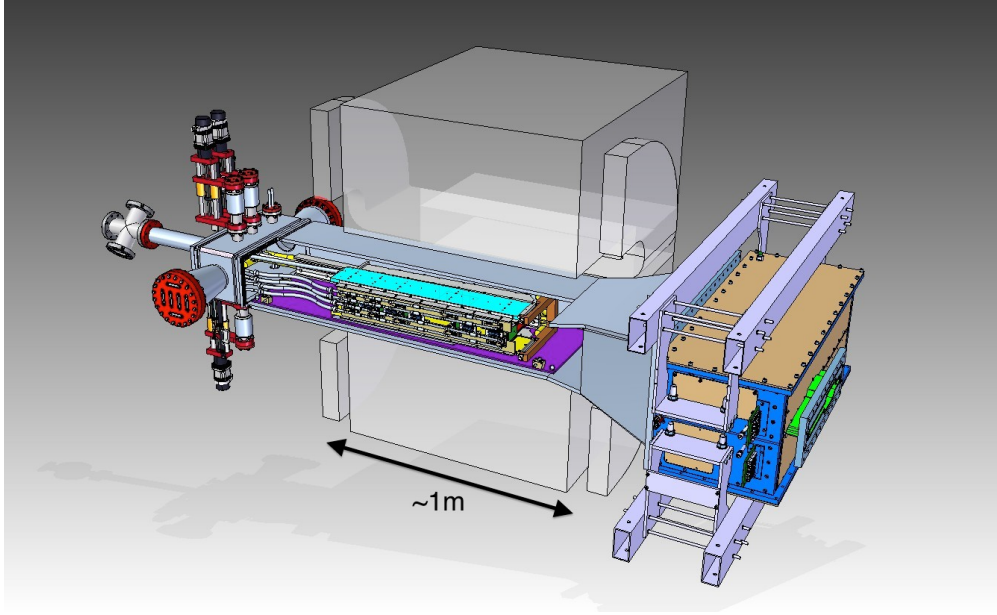


Figure 1: Rendering of the HPS Test Run apparatus installed on the beam line.

Table 1: Overview of the coverage, segmentation and performance of the HPS Test Run detector. The  $\sigma_{d0}$  is the track impact parameter resolution of the SVT at the nominal iron target position.  $\sigma_{pos}$  is the estimated position resolution perpendicular to the strip direction on the silicon sensors of the SVT.

System	Coverage (mrad)	# channels	ADC (bit)	# layers	Segmentation	Time resolution (ns)	Performance
SVT	$15 < \theta_y < 70$ (5 hits)	12780	14	5 (stereo layers)	$30 \mu\text{m}$ (sense) $60 \mu\text{m}$ (readout) ( $\sigma_{pos} \approx 6 \mu\text{m}$ )	2.5	$\sigma_{d0,y} \approx 100 \mu\text{m}$ $\sigma_{d0,x} \approx 300 \mu\text{m}$ $\sigma_{d0,z} \approx 1 \text{ mm}$
ECal	$15 < \theta_y < 60$	442	12	1	$1.33 \times 1.33 \text{ cm}^2$ $1.6 \times 1.6 \text{ cm}^2$	4 (trigger)	$\sigma(E)/E \approx 4.5\%/\sqrt{E}$ Ref. [13, 14, 15]

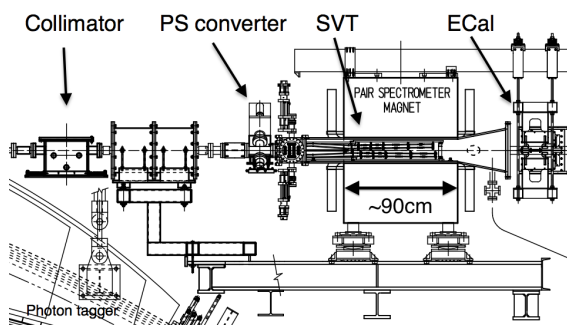


Figure 2: Layout of the HPS parasitic run.

The photon beam was generated in the interaction of 5.5 GeV electrons with a  $10^{-4} X_0$  gold radiator located  $\approx 9$  m upstream of the PS. The primary beam and scattered electrons are deflected away from detectors by the dipole magnet of the photon tagging system. During the dedicated HPS Test Run period, the collimated (6.4 mm diameter) photon beam passes through the PS pair converter gold foil and later the HPS system. The PS pair converter was located  $\approx 77$  cm upstream of the first layer of the SVT.

Data was taken on three different converter thicknesses with photon fluxes between  $0.4-1.3 \times 10^8/\text{s}$  at photon energies between 0.55 and 5.5 GeV produced by a 30-90 nA electron beam. Data was measured for both polarities of the PS dipole magnet. The photon beam line during the HPS Test Run produced a relatively large number of  $e^+e^-$  pairs originating upstream

Converter thickn. (% $X_0$ )	Duration (s)	$e^-$ on radiator ( $\mu\text{C}$ )
0	1279	88.1
0.18	2640	193.5
0.45	2149	140.7
1.6	911	24.4

Table 2: Measured integrated currents for the dedicated photon runs.

of the converter position. This contribution was measured during data taking with “empty” converter runs, i.e. removing the converter but with all other conditions the same. The runs taken during the time dedicated to HPS Test Run are summarized in Table 2.

#### 4. Silicon Vertex Tracker

The Silicon Vertex Tracker (SVT) enables efficient reconstruction of charged particles and precise determination of their trajectories. This allows  $A'$  decays to be distinguished from background via simultaneous measurements of the invariant mass of  $e^+e^-$  decay products and the position of decay vertices downstream of the target.

The design of the SVT is primarily driven by physics requirements and constraints from the environment at the interaction region. The  $A'$  decay products have momenta in the range of 0.4-2.0 GeV/c (for a 2.2 GeV beam), so multiple scattering dominates mass and vertexing uncertainties for any possible material budget. The SVT must therefore minimize the amount of material in the tracking volume. The signal yield for long-lived  $A'$  is very small, so the rejection of prompt vertices must be exceedingly pure, on the order of  $10^{-7}$ , in order to eliminate all prompt backgrounds. To achieve the required vertexing performance the first layer of the SVT must be placed no more than about 10 cm downstream of the target. At that distance, it is found that the active region of a sensor can be placed as close as 1.5 mm from the center of the beam, defining the 15 mrad “dead zone” mentioned previously, to maximize low-mass  $A'$  acceptance with decay products nearly collinear with the beam axis. At the edge of this “dead zone”, the radiation dose approaches  $10^{15}$  electrons/cm<sup>2</sup>/month, or roughly  $3 \times 10^{13}$  1 MeV neutron equivalent/cm<sup>2</sup>/month [16], requiring the sensors to be actively cooled. Meanwhile, very low-energy delta rays from beam-gas interactions would multiply the density of background hits, so the SVT must operate inside the beam vacuum. Finally, in order to protect the sensors, the detector must be movable

so that it can be retracted during periods of uncertain beam conditions or beam tuning.

A mass resolution of 2.5% is adequate to extend a bump-hunt search for an  $A'$  into virgin territory. For running at 2.2 GeV, this translates into a requirement for track momentum ( $p$ ) resolution of 4-5% and angular resolution of about 2 mrad/ $p$ (GeV/c) [11]. Multiple Coulomb scattering dominates both the mass and vertexing uncertainties, relaxing the spatial hit resolution requirement to < 100  $\mu\text{m}$  (50  $\mu\text{m}$ ) in the bend (non-bend) plane.

High background occupancies, up to 4 MHz/mm<sup>2</sup> locally, in the region closest to the beam result from beam electrons undergoing multiple scattering in the target. These background hits are rejected by requiring reconstruction of the hit time relative to the trigger with 2 ns resolution.

##### 4.1. Layout

The layout of the SVT is summarized in Table 3 and rendered in Figure 3. Each of the layers is comprised of a pair of closely-spaced silicon microstrip sensors mounted back-to-back to form a module. A 100 mrad stereo angle is used in the first three layers to provide higher-resolution 3D space points for vertexing. Using 50 mrad in the last two layers breaks the tracking degeneracy of having five identical layers and minimizes fakes from ghost hits to improve pattern recognition. Altogether, the SVT has 20 sensors for a total of 12780 readout channels.

Layer	1	2	3	4	5
$z$ from target (cm)	10	20	30	50	70
Stereo angle (mrad)	100	100	100	50	50
Bend res. ( $\mu\text{m}$ )	$\approx 60$	$\approx 60$	$\approx 60$	$\approx 120$	$\approx 120$
Non-bend res. ( $\mu\text{m}$ )	$\approx 6$	$\approx 6$	$\approx 6$	$\approx 6$	$\approx 6$
# of sensors	4	4	4	4	4
Dead zone (mm)	$\pm 1.5$	$\pm 3.0$	$\pm 4.5$	$\pm 7.5$	$\pm 10.5$
Power cons. (W)	6.9	6.9	6.9	6.9	6.9

Table 3: Layout of the SVT.

The SVT is built in two separate halves that are mirror reflections of one another about the plane of the nominal electron beam. Each half consists of five modules mounted on a support plate that provides services to the modules and allows them to be moved as a group relative to the dead zone. The two halves of the tracker are connected to hinges mounted on a C-shaped support

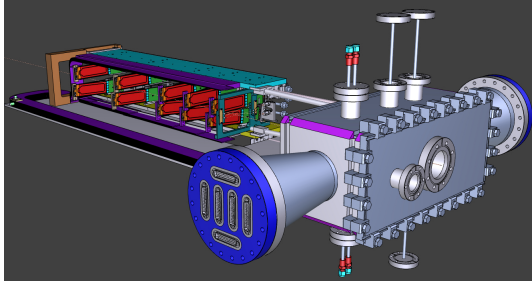


Figure 3: A rendering of the SVT showing the modules on their support plates held by the hinged C-support on the left and the motion levers on the right. The sensors are shown in red and the hybrid readout boards in green. The beam enters from the right through a vacuum box with flanges for services.

just beyond the last layer that defines the nominal spacing between the upper and lower halves of the tracker. A shaft attached to each support plate in front of layer one extends upstream and connects to a linear shift that transfers motion into the vacuum box through bellows to open and close the two halves around the dead zone. The C-support is mounted to an aluminum baseplate that defines the position of the SVT with respect to the vacuum chamber. Figure 4 shows a photograph of both completed detector halves prior to final assembly.



Figure 4: Both halves of the HPS Test Run SVT after final assembly at SLAC. The cooling manifolds and integrated cable runs are clearly seen.

297

#### 298 4.2. Components

299 The sensors for the SVT are  $p+$ -on- $n$ , single-sided,  
300 AC-coupled, polysilicon-biased microstrip sensors fab-  
301 ricated on  $<100>$  silicon and have 30 (60)  $\mu\text{m}$  sense  
302 (readout) pitch over their  $4 \times 10 \text{ cm}^2$  surface. This  
303 sensor technology was selected to match the require-  
304 ment of  $< 1\% X_0$  per layer, single-hit resolution bet-

305 ter than 50  $\mu\text{m}$  and tolerance of a radiation dose of ap-  
306 proximately  $1.5 \times 10^{14}$  1 MeV neutron equivalent/ $\text{cm}^2$   
307 for a six month run. The sensors, produced by Ham-  
308 a-matsu Photonics Corporation, were originally meant  
309 for the cancelled Run 2b upgrade of the DØ exper-  
310 iment [17] which satisfied the requirement that the tech-  
311 nology must be mature and available within the time and  
312 budget constraints.

313 Despite having only small spots with very high occu-  
314 pancy (up to 4 MHz/mm $^2$ ) closest to the primary beam,  
315 the rates are still high and lowering the peak occupancy  
316 to approximately 1% for tracking requires a trigger win-  
317 dows and hit time tagging of roughly 8 ns. The ECal  
318 readout and trigger described in Sec. 5.3 can achieve  
319 such resolution. To reach this performance the sensors  
320 for the SVT are readout by the APV25 ASIC developed  
321 for the CMS experiment at CERN [18]. The APV25  
322 ASIC can capture successive samples of the shaper out-  
323 put in groups of three at a sampling rate of approxi-  
324 mately 40 MHz. By fitting the known  $CR-RC$  shaping  
325 curve to these samples, the initial time of the hit can  
326 be determined to a precision of 2 ns for S/N $\approx 25$  [19].  
327 For electron beam running, six-sample readout and the  
328 shortest possible shaping time (35 ns) are used to best  
329 distinguish hits that overlap in time. The APV25 ASICs  
330 are hosted on simple FR4 hybrid readout boards out-  
331 side the tracking volume with a short twisted-pair pig-  
332 tail cable to provide power, configuration, and signal  
333 readout. Along with a single sensor, these are glued  
334 to a polyimide-laminated carbon fiber composite back-  
335 ing making up a half-module. A window is machined  
336 in the carbon fiber leaving only a frame around the pe-  
337 riphery of the silicon to minimize material. A 50  $\mu\text{m}$   
338 sheet of polyimide is laminated to the surface of the car-  
339 bon fiber with 1 mm overhang at all openings to ensure  
340 good isolation between the back side of the sensor, car-  
341 rying high-voltage bias, and the carbon fiber which is  
342 held near ground.

343 The sensor modules for the SVT consist of a pair  
344 of identical half-modules, sandwiched back-to-back  
345 around an aluminum cooling block at one end and a sim-  
346 ilar PEEK spacer block at the other. Figure 5 shows a  
347 single module after assembly. The cooling block pro-  
348 vides the primary mechanical support for the module as  
349 well as cooling via copper tubes pressed into grooves  
350 in the plates. The spacer block defines the spacing be-  
351 tween the sensors at the far end of the module, stiffens  
352 the module structure, and improves the stability of the  
353 sensor alignment. The average support material in the  
354 tracking volume is approximately 0.06%  $X_0$  per double-  
355 sided module for a total material budget of 0.7% per  
356 layer.

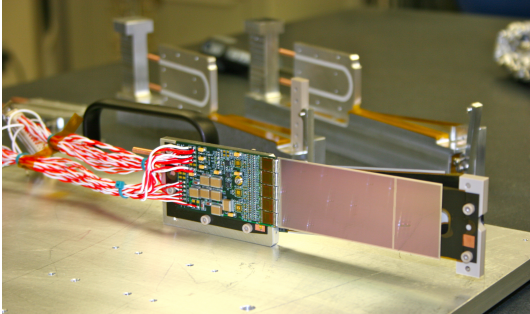


Figure 5: A prototype module assembly (foreground) with the 50 mrad (left) and 100 mrad (right) module assembly fixtures in the background. A pair of cooling blocks and a spacer block can be seen on the fixtures.

The total SVT power consumption budget of about 50 W is removed by a water/glycol mixture circulated through a flexible manifold attached to the copper tubes in the cooling blocks. During the HPS Test Run the sensors were operated at around 23° C. The power consumption is dominated by five APV25 ASICs on each hybrid board consuming approximately 2 W, the radiant heat load is less than 0.5 W per sensor and leakage current is only significant in a small spot after irradiation.

#### 4.3. Production, Assembly and Shipping

Hybrids with APV25 ASICs underwent quick qualification testing and each half-module was run at low temperature ( $\approx 5^\circ \text{C}$ ) and fully characterized for pedestals, gains, noise and time response after assembly. Of 29 half-modules built, 28 passed qualification testing, leaving eight spare modules after completion of the SVT. Only sensors capable of 1000 V bias voltage without breakdown were used. Full-module assembly and mechanical surveys were performed at SLAC before final assembly, testing and shipping of the SVT to JLab. A custom shipping container with nested crates and redundant isolation for shock and vibration was built in order to safely send the partly assembled SVT to JLab. At JLab, the entire SVT was integrated with the full data acquisition and the power supplies before moving the module-loaded support plates to Hall B for final mechanical assembly and installation inside of the vacuum chamber.

#### 4.4. Alignment

The SVT was aligned using a combination of optical, laser and touch probe surveys at SLAC and JLab. The optical survey of individual modules with a precision of

a few  $\mu\text{m}$  was combined with a touch-probe survey of the overall SVT support structure, with 25–100  $\mu\text{m}$  precision, to locate the silicon sensor layers with respect to the support plates and the mechanical survey balls on the base plate. After full assembly and installation of the SVT at JLab, a mechanical survey of the SVT base plate position inside the pair spectrometer vacuum chamber is used to determine the global position of the SVT with respect to the CEBAF beam line. The resulting survey-based alignment has the position of the silicon sensors correct to within a few hundred microns measured from tracks in the HPS Test Run data. A more sophisticated global track-based alignment technique to reach final alignment precision well below 50  $\mu\text{m}$  is being developed.

## 5. Electromagnetic Calorimeter

The electromagnetic calorimeter (ECal), installed downstream of the PS dipole magnet, performs two essential functions for the experiment: it provides a trigger signal to select what events to read out from the detector sub-systems and is used to identify electrons and positrons. The technology and design choices are largely driven by the need for a compact forward design covering the SVT A' acceptance and the ability to measure the energy and positions of electrons and positrons with energy between 0.5 and 6.6 GeV. It needs granularity and signal readout speed to handle 1 MHz/cm<sup>2</sup> of electromagnetic background as well as good radiation hardness. Even modest energy resolution is adequate for triggering. HPS requires better energy resolution,  $\sigma(E)/E < 5\%/\sqrt{E}$ , so that the ECal energy measurement can be used in combination with that from the SVT to improve the overall momentum resolution.

The PbWO<sub>4</sub> crystal inner calorimeter of the CLAS detector [13, 14, 15], in operation since 2005 in Hall B, meets all the requirements set by HPS. The modules from this calorimeter have been subsequently repurposed for HPS.

### 5.1. Components

The ECal module shown in Figure 6 is based on a tapered 160 mm long PbWO<sub>4</sub> crystal with a 13.3 × 13.3 mm<sup>2</sup> (16 × 16 mm<sup>2</sup>) front (rear) face wrapped in VM2000 multilayer polymer mirror film. The scintillation light yield, approximately 120 photons/MeV, is read out by a 5×5 mm<sup>2</sup> Hamamatsu S8664-55 Avalanche Photodiode (APD) with 75% quantum efficiency glued to the rear face surface using MeltMount 1.7 thermal plastic adhesive. This results in about eight

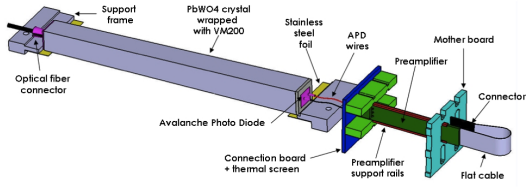


Figure 6: A schematic view of an ECal module.

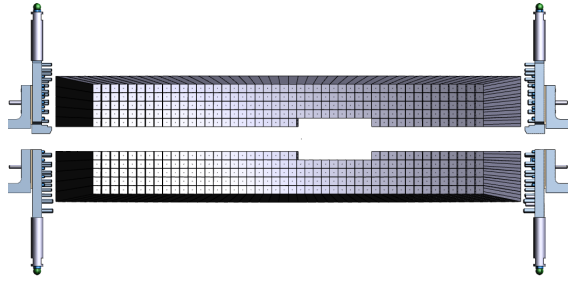


Figure 7: Rendered layout view of the ECal looking downstream.

437 photoelectrons/MeV which needs to be amplified before  
 438 being fed into the JLab Flash ADC [20] (FADC) board  
 439 for digitization and processing. The maximum energy  
 440 deposited in a crystal is expected to be 4.2 GeV which  
 441 needs to match the input range of the FADC. The rel-  
 442 atively low gain of the APD ( $\sim 200$ ) was compensated  
 443 with custom-made preamplifier boards, that provide fur-  
 444 ther amplification to match the 2 V dynamic range of the  
 445 FADC. The ADC has 12-bit resolution. Gains are ad-  
 446 justed to give about 1 ADC count/MeV. This dynamic  
 447 range is adequate to measure the 10 MeV noise level as  
 448 well as the the maximum energy expected in a single  
 449 crystal, about 4 GeV.

## 450 5.2. Layout

451 Similar to the SVT, the ECal is built in two separate  
 452 halves that are mirror reflections of one another about  
 453 the plane of the nominal electron beam to avoid inter-  
 454 fering with the 15 mrad “dead zone”. As shown in Fig-  
 455 ure 7, the 221 modules in each half, supported by alu-  
 456 minium support frames, are arranged in rectangular for-  
 457 mation with five layers and 46 crystals/layer except for  
 458 the layer closest to the beam where nine modules were  
 459 removed to allow a larger opening for the outgoing elec-  
 460 tron and photon beams. Each half was enclosed in a  
 461 temperature controlled box ( $< 1^\circ \text{ F}$  stability and  $< 4^\circ \text{ F}$   
 462 uniformity) to stabilize the crystal light yield and the op-  
 463 eration of the APDs and its preamplifiers. Four printed  
 464 circuit boards mounted on the backplane penetrated the  
 465 enclosure and were used to supply the  $\pm 5$  V operating  
 466 voltage for the preamplifiers, 400 V bias voltage to the  
 467 APDs, and to read out signals from the APDs. Each half  
 468 of the ECal was divided into 12 bias voltage groups with  
 469 a gain uniformity of about 20%.

470 During the HPS Test Run, both halves were held in  
 471 place by four vertical bars attached to a rail above, plac-  
 472 ing the front face of the crystals 147 cm from the up-  
 473 stream edge of the magnet, with a 8.7 cm gap between  
 474 the innermost edge of the crystals in the two halves.

## 475 5.3. Signal Readout

476 After a 2:1 signal splitter, 1/3 of an amplified APD  
 477 signal was fed to a single channel of a FADC board.  
 478 2/3 of the signal was sent to a discriminator module  
 479 and then to a TDC for a timing measurement. The  
 480 FADC boards are high speed VXS modules digitizing  
 481 up to 16 APD signals at 250 MHz and storing samples  
 482 in 8  $\mu\text{s}$  deep pipelines with 12-bit resolution. When  
 483 a trigger is received, the part of the pipeline from five  
 484 samples before and 30 after the signal which crossed a  
 485 programmable threshold (for the HPS Test Run this was  
 486 set to  $\approx 70$  MeV) are summed and stored in a 17-bit reg-  
 487 ister for readout. In addition a 4 ns resolution timestamp  
 488 of the threshold crossing is reported in the readout for  
 489 each pulse. This scheme significantly compresses the  
 490 data output of the FADC. During offline data analysis, a  
 491 calibrated pedestal value is subtracted to obtain the ac-  
 492 tual summed energy. Two 20-slot VXS crates with 14  
 493 (13) FADC boards were employed in the HPS Test Run  
 494 to read out the top (bottom) half of the ECal.

## 495 6. Trigger and Data Acquisition

496 The data acquisition (DAQ) system handles acquisi-  
 497 tion of data from the ECal and SVT sub-detectors with  
 498 two DAQ architectures. The SVT DAQ is based on Ad-  
 499 vanced Telecom Communications Architecture (ATCA)  
 500 hardware while the ECal uses VMEbus Switched Serial  
 501 (VXS) based hardware. Data from the sub-detectors are  
 502 only read out when a trigger signal from the trigger sys-  
 503 tem is received.

### 504 6.1. Trigger System

505 The trigger system is designed to select time coinci-  
 506 dences of electromagnetic clusters in the top and bottom  
 507 halves of the ECal which meets kinematic conditions  
 508 satisfied by  $A'$  decays and minimize backgrounds. The

509 trigger system needs to be essentially dead-time free,  
 510 handle rates up to 50 kHz, and supply a trigger signal  
 511 which jitters < 8 ns from the actual event time in or-  
 512 der to minimize backgrounds from out-of-time hits in  
 513 the SVT. Figure 8 shows a schematic overview of each  
 514 stage of the system. Each channel on the FADC board  
 515 has an independent data path to send 5-bit pulse energy  
 516 and 3-bit pulse arrival time information every 32 ns to  
 517 a Crate Trigger Processor board (CTP), which is in the  
 518 same crate. The 3-bit pulse arrival time allows the trig-  
 519 ger to know the pulse timing at 4 ns resolution. Contrary  
 520 to the readout path described in Sec. 5.3, this energy is  
 521 a pedestal-subtracted time-over-threshold sum with pro-  
 522 grammable offsets and minimum threshold discrimina-  
 523 tor for each channel. With input from all FADC chan-  
 524 nels, i.e. one half of the ECal, the CTP performs cluster  
 525 finding and calculates cluster energy and timing infor-  
 526 mation. The 3x3 fixed-window, highly parallel, FPGA-  
 527 based cluster algorithm simultaneously searches for up  
 528 to 125 clusters with energy sum larger than the pro-  
 529 grammable energy threshold set to about 270 MeV. This  
 530 high threshold didn't hurt the trigger rate rate studies  
 531 for the HPS Test run since only clusters with high ener-  
 532 gies were studied but for HPS this threshold will need to  
 533 be lower. Crystals in the fixed-window are included in  
 534 the sum if the leading edge of the pulse occurred within  
 535 a 32 ns time window to take into account clock skew  
 536 and jitter throughout the system. The CTP only accepts  
 537 clusters with the locally highest energy 3x3 window  
 538 to deal with overlapping and very large clusters. The  
 539 Sub-System Processor board (SSP) receives the clusters  
 540 from the top and bottom half CTP at a maximum rate  
 541 of 250 MHz and searches for pairs of clusters in an 8 ns  
 542 wide coincidence window. The SSP sends triggers to  
 543 the trigger supervisor (TS), which generates all the nec-  
 544 essary signals and controls the entire DAQ system read-  
 545 out through the trigger interface units installed in every  
 546 crate that participate in the readout process.



Figure 8: Block diagram of the ECAL trigger system consisting of the FADC that samples and digitizes signals for each detector channel and sends them for cluster finding in the CTP. The CTP clusters are sent to the SSP where the final trigger decision is taken based on pairs of clusters in both halves of the ECal. The decision is sent to the Trigger Supervisor (TS) that generates the necessary signals to read out the sub-detectors.



Figure 9: The SVT DAQ COB board with four data processing daughter cards (DPMs) visible on the left side.

547 The trigger system is free-running and driven by the  
 548 250 MHz global clock and has essentially zero dead  
 549 time at the occupancies expected for HPS. The trigger  
 550 supervisor can apply dead time if necessary, for example  
 551 on a ‘busy’ or ‘full’ condition from the front-end elec-  
 552 tronics. The system is designed to handle trigger rates  
 553 above 50 kHz and has a latency set to  $\approx 3 \mu\text{s}$  to match  
 554 that required by the SVT APV25 ASIC.

555 During most of the HPS Test Run, the trigger system  
 556 required only a single cluster in either the top or bottom  
 557 ECal halves resulting in rates below 2 kHz. However,  
 558 the trigger system was tested to rates above 100 kHz by  
 559 lowering thresholds.

## 6.2. SVT Data Acquisition

560 The purpose of the SVT DAQ is to support the con-  
 561 tinuous 40 MHz readout and processing of signals from  
 562 each of the 20 silicon strip sensors of the SVT. The data  
 563 for each strip channel, six samples of the signal, needs  
 564 to be transferred to the JLab DAQ for those events se-  
 565 lected by the trigger at rates up to 50 kHz and with data  
 566 transfer rates up to 100 MB/s.

567 The SVT DAQ is based on the Reconfigurable Clus-  
 568 ter Element (RCE) and cluster interconnect concept de-  
 569 veloped at SLAC as generic building blocks for DAQ  
 570 systems. The RCE is a generic computational build-  
 571 ing block, housed on a separate daughter card called  
 572 Data Processing Module (DPM), that is realized on an  
 573 ATCA front board called the Cluster On Board (COB),  
 574 as shown in Figure 9. The first generation RCE used in  
 575 the HPS Test Run consisted of a Virtex 5 FPGA with  
 576 1 GB of DDR3 RAM. A schematic overview of the sys-  
 577 tem is shown in Figure 10. The analog outputs of up  
 578 to 12 SVT half-modules (60 APV25 ASICs) are digi-  
 579 tized on the Rear-Transition-Module (RTM), a custom  
 580 board on the back side of the ATCA crate, interfacing  
 581 the HPS-specific readout to the generic DAQ compo-  
 582 nents on the COB. A preamplifier converts the APV25  
 583

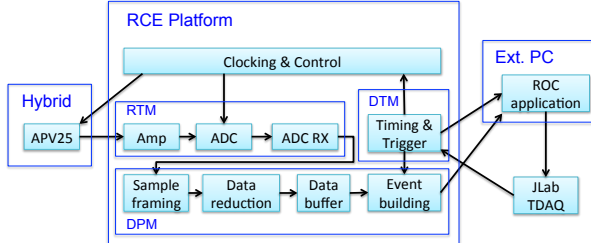


Figure 10: Block diagram overview of the SVT DAQ.

584 ASIC differential current output to a different voltage  
 585 output scaled to the sensitive range of a 14-bit ADC  
 586 operating at the system clock of 41.667 MHz. The  
 587 RTM is organized into four sections with each section  
 588 supporting three SVT half-module hybrids (15 APV25  
 589 ASICs). The RTM also includes a 4-channel fiber-optic  
 590 module and supporting logic which is used to interface  
 591 to the JLab trigger system supervisor. Each section of  
 592 the RTM is input to a DPM which apply thresholds for  
 593 data reduction and organizes the sample data into UDP  
 594 datagrams. The DPM also hosts an I<sup>2</sup>C controller used  
 595 to configure and monitor the APV25 ASICs. A single  
 596 ATCA crate with two COB cards was used, one supporting  
 597 four DPMs and one supporting three DPMs and one  
 598 DPM that is configured as the trigger and data transmis-  
 599 sion module. The two COB cards and their DPMs are  
 600 interconnected with a 10 Gb/s switch card [21] which  
 601 also hosts two 1 Gb/s Ethernet interfaces to the external  
 602 SVT DAQ PC.

603 The external PC supports three network interfaces:  
 604 two standard 1 Gb/s Ethernet and one custom low-  
 605 latency data reception card. The first is used for slow  
 606 control and monitoring of the eight DPM modules and  
 607 the second serves as the interface to the JLAB data ac-  
 608 quisition system. The third custom low-latency network  
 609 interface is used to receive data from the ATCA crate  
 610 and supports a low latency, reliable TTL trigger ac-  
 611 knowlidge interface to the trigger DPM. This PC hosts  
 612 the SVT control and monitoring software as well as the  
 613 readout controller application used to interface with the  
 614 JLab DAQ.

615 In order to minimize cable length for the analog  
 616 APV25 ASIC output signal the ATCA crate was lo-  
 617 cated approximately 1 m from the beam line, next to  
 618 the cable vacuum feed-throughs. Before shielding with  
 619 lead-blankets and borated polyethylene was arranged,  
 620 we observed two failures of normally reliable ATCA  
 621 crate power supplies, time-correlated to beam instabili-  
 622 ties.

623 Although trigger rates during the HPS Test Run were  
 624 significantly lower, this system was tested at trigger  
 625 rates up to 20 kHz and 50 MB/s. With optimized event  
 626 blocking and improved Ethernet bandwidth, together  
 627 with utilizing the overlapping readout and trigger func-  
 628 tionality of the APV25 ASIC, the system is capable of  
 629 being read out at 50 kHz trigger rate.

### 630 6.3. General Data Acquisition and Online Computing

631 Every crate participating in the readout process con-  
 632 tains a Readout Controller (ROC) that collects digitized  
 633 information, processes it, and sends it on to the event  
 634 builder. For the ECal, both VXS crates run ROC ap-  
 635 plications in a single blade Intel-based CPU module run-  
 636 ning CentOS Linux OS. For the SVT DAQ, the ROC  
 637 application runs on the external PC under RHEL. The  
 638 event builder assembles information from the ROCs into  
 639 a single event which is passed to the event recorder that  
 640 writes it to a RAID5-based data storage system capa-  
 641 ble of handling up to 100 MB/s. The event builder and  
 642 other critical components run on multicore Intel-based  
 643 multi-CPU servers. The DAQ network system is a net-  
 644 work router providing 10 Gb/s high-speed connection to  
 645 the JLab computing facility for long-term storage. For  
 646 the HPS Test Run, both the SVT and ECal ROC had a  
 647 1 Gb/s link to the network router.

## 648 7. Reconstruction and Performance

649 While dedicated electron beam was precluded for the  
 650 HPS Test Run the short dedicated photon beam run al-  
 651 lowed the study of some of the key performance param-  
 652 eters for HPS and the trigger rates expected during elec-  
 653 tron beam running. This section documents the perfor-  
 654 mance and discusses the implications of these results for  
 655 HPS.

### 656 7.1. SVT Performance

657 For the duration of the HPS Test Run all SVT mod-  
 658 ules and APV25 ASICs were configured to their nomi-  
 659 nial operating points [22] with all sensors reverse-biased  
 660 at 180 V. The sensors were operated within a temper-  
 661 ature range of 20 – 24°C. Approximately 97% of the  
 662 12,780 SVT channels were found to be operating nor-  
 663 mally; the fraction of dead or noisy channels varied  
 664 from 2.4% to 4.7% throughout the HPS Test Run. Most  
 665 of these losses were due to 2-4 misconfigured APV25  
 666 ASICs, a known noisy half-module and problems in two  
 667 particular APV25 ASICs.

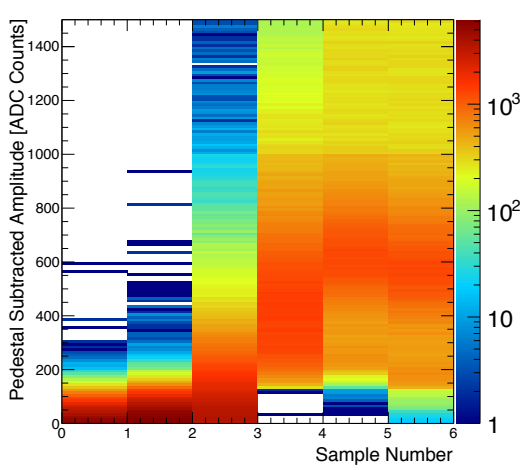


Figure 11: Accumulation of six pedestal-subtracted samples from individual SVT channels associated with hits on tracks.

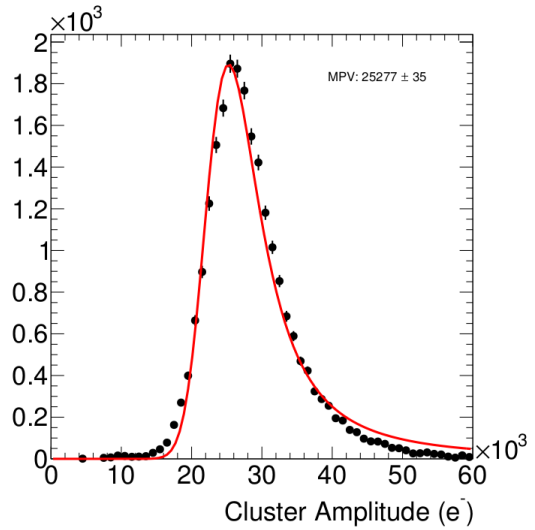


Figure 12: The cluster charge distribution for hits associated with a track follow the characteristic Landau shape.

### 668 7.1.1. Cluster and Hit Reconstruction

669 Track reconstruction in the SVT puts stringent re-  
 670 quirement on the clustering and hit reconstruction. The  
 671 multiple scattering in the tracking material dominates  
 672 the uncertainty in the track parameter estimation and ef-  
 673 fectively determines the roughly  $50 \mu\text{m}$  ( $100 \mu\text{m}$ ) re-  
 674 quirement on the spatial hit resolution in the non-bend  
 675 (bend) plane. The high occupancy due to multiple scat-  
 676 tered beam electrons in the target close to the beam re-  
 677 quires a hit time resolution of 2 ns to efficiently reject  
 678 out-of-time hits in HPS. Both the hit time, based on a  
 679 fit to the APV25 ASIC pulse shape, and the spatial po-  
 680 sition reconstruction rely on having  $S/N$  around 25 for  
 681 the sensors used in HPS.

682 After a trigger is received, the amplitude of every  
 683 APV25 ASIC is sampled and digitized in the six con-  
 684 secutive time bins associated with the trigger time. A  
 685 data reduction algorithm is applied requiring three out  
 686 of six samples to be above two times the noise level and  
 687 that the third sample is larger than the second or that  
 688 the fourth sample is larger than the third. The typical,  
 689 pedestal subtracted, pulse shape obtained is shown in  
 690 Figure 11. As the figure demonstrates, the SVT was  
 691 well timed-in to the trigger with the rise of the pulse at  
 692 the 3rd sampling point. In order to find the time,  $t_0$ , and  
 693 amplitude of each hit, the six samples from each chan-  
 694 nel are fitted to an ideal  $CR - RC$  function. Note that  
 695 in the HPS Test Run the APV25 ASICs were operating  
 696 with a 50 ns shaping time. These hits are passed through  
 697 a simple clustering algorithm which forms clusters by

698 grouping adjacent strips with the position of a cluster on  
 699 the sensor determined by the amplitude-weighted mean.  
 700 With a linear gain up to  $\approx 3$  MIPs, the cluster charge  
 701 for hits associated with a track follow the characteris-  
 702 tic Landau shape, see Figure 12. A noise level between  
 703  $1.1 - 1.5 \times 10^3$  electrons was established through mul-  
 704 tiple calibration runs giving a  $S/N$  of 21 – 25, in line  
 705 with the requirement for HPS. Radioactive source tests  
 706 were used to provide the absolute charge normalization.  
 707 After clustering hits on a sensor, the hit time for each  
 708 cluster is computed as the amplitude-weighted average  
 709 of the individually fitted  $t_0$  on each channel. The  $t_0$   
 710 resolution is studied by comparing the cluster hit time with  
 711 the average of all cluster hit times on the track shown in  
 712 Figure 13. After correcting for offsets from each sensor  
 713 (time-of-flight and clock phase) and accounting for the  
 714 correlation between the  $t_0$  and track time, the extracted  
 715  $t_0$  resolution is 2.6 ns. This is somewhat worse than  
 716 the approximately 2 ns resolution expected for  $S/N=25$   
 717 which we attribute to the true pulse shape differing from  
 718 our idealized fit function which will be improved in the  
 719 future [23]. Reducing the APV25 ASIC pulse shaping  
 720 time to 35 ns will also improve time resolution. These  
 721 results show that HPS can operate with the six sam-  
 722 ple readout mode of the APV25 ASIC and achieve time  
 723 resolution adequate for pileup rejection during electron  
 724 running in HPS.

725 Good agreement was obtained between observed and  
 726 simulated occupancies after taking into account dead or

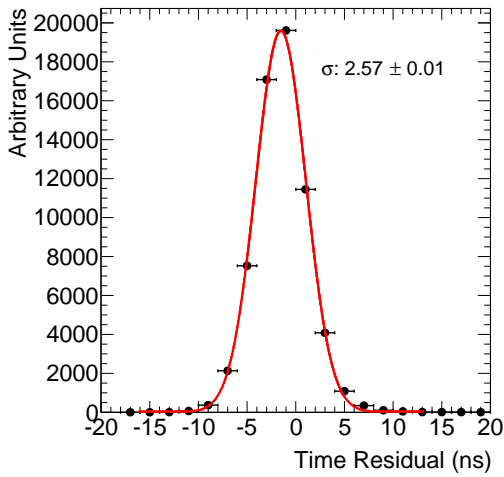


Figure 13: The residual of individual cluster times with the average of all clusters on the track.

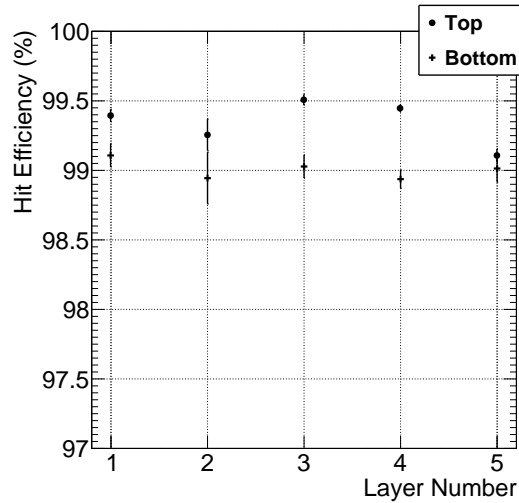


Figure 14: The hit reconstruction efficiency as a function of detector layer.

noisy channels. The hit reconstruction efficiency was estimated by measuring the number of good tracks with a hit close to the interpolated position on a given sensor that was excluded from the track fit. Tracks which intersect regions with known bad channels or pass very close to the edge region were excluded. The hit reconstruction efficiency, see Figure 14, was measured to be above 98% and fairly uniform across the SVT.

The spatial resolution of similar microstrip sensors is well established by test beam data, against which the charge deposition model in the simulation is validated. This resolution can be parameterized as a function of the total signal to single-strip noise and the crossing angle of tracks through the sensor. The single-hit resolution for charged particles with  $S/N > 20$ , as demonstrated here, is relatively constant at approximately  $6 \mu\text{m}$  for tracks that enter approximately normal to the sensors as in HPS. This resolution is significantly better than the requirement for reaching the mass and vertex resolutions required for HPS.

#### 7.1.2. Momentum and Vertexing Resolution

Good track reconstruction performance is crucial to HPS. Simulations show that track momentum resolution of 4-5% is needed to achieve the desired  $A'$  mass resolution. The precise reconstruction of the production vertex to reject prompt QED background requires impact parameter resolutions between  $100\text{-}250 \mu\text{m}$  for tracks between  $0.5\text{-}1.7 \text{ GeV}/c$ . These key performance parameters were studied in the HPS Test Run by selecting

$e^+e^-$  pairs from photon conversions. Pairs of oppositely charged tracks, one in the top and one in the bottom half of the SVT, with momentum larger than  $400 \text{ MeV}/c$  were selected and basic distributions of pair production kinematics were studied. The kinematics are relatively well reproduced as shown in Figure 15.

The expected momentum resolution from simulation is between 4-5% for tracks in the momentum range of the HPS Test Run. By comparing the shapes of the kinematic distributions for data and simulation, we estimate an agreement with the nominal scale and resolution to within 10%.

In the HPS Test Run, as well as in electron running with HPS, the dominant source of uncertainty in the tracking and vertexing is multiple Coulomb scattering. For the vertexing performance the foremost difference between the HPS Test Run and HPS is that the HPS Test Run target is 67 cm further upstream, so tracks must be extrapolated nearly eight times as far as in HPS, giving almost collinear tracks in the detector. The increased lever arm over which tracks are extrapolated worsens the resolution up to a factor of eight (depending on momentum) compared to what is achieved at the nominal electron target position for HPS. Figure 16 shows the horizontal and vertical positions of the extrapolated track at the converter position. While residual alignments show small shifts, the good agreement between data and simulated events of the widths indicates a good

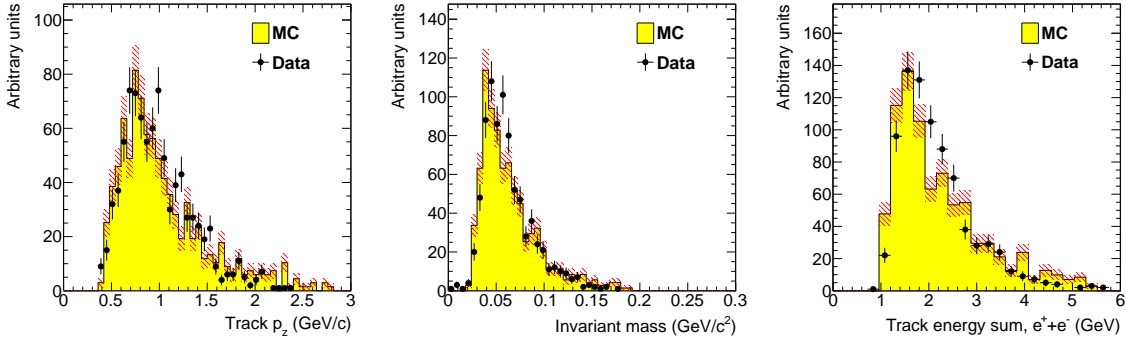


Figure 15: Kinematic distributions for  $e^+e^-$  pairs selected by opposite charged tracks in the top and bottom half of the tracker: track momentum in the top half of the SVT (left), invariant mass (middle) and the sum of the track energy for the pair (right).

understanding of the material budget and distribution in the SVT. Having the dominant contribution to the vertex resolution approximately right demonstrates that the Gaussian part of the vertex resolution in HPS, with a target at 10 cm, will be as calculated.

### 7.2. ECal Performance

During the HPS Test Run 385 out of 442 modules (87%) were used in offline reconstruction, 39 modules were disabled or not read out (no FADC channel available, no APD bias voltage or masked out due to excessive noise) and 18 were masked offline due to noise.

The integrated pulse of each FADC channel was converted to energy by subtracting a pedestal and applying a conversion factor to convert ADC counts to energy. The pedestals are measured using special runs where each trigger records 100 samples of signals from the APDs with 4 ns between each sample. The pedestals were extracted from the part of the window before the actual hit in the calorimeter. Modules with signal above the threshold are clustered using a simple algorithm similar to the one deployed for the trigger (see Sec. 6.1). Due to the high effective crystal readout threshold of 73 MeV the average number of crystals in a cluster was only about three and the simple clustering algorithm worked well for reconstruction of the detected shower energy. An average noise level of approximately 15 MeV per crystal was measured in special pedestal runs. The high crystal noise level and effective threshold didn't hurt the trigger rate studies in the HPS Test Run as clusters with high energy were used for the analysis. For HPS the noise level and threshold will be lowered to improve energy resolution and to allow triggering on cosmics to improve calibration.

The ratio of the ECal cluster energy  $E$  to the momentum  $p$  of a matched track in the SVT was used to de-

termine the conversion factors from ADC counts to energy. To compare data and simulation, all inoperable or noisy channels in the SVT and ECal were disabled in both data and simulation so that any efficiency or bias that affect the data should be reflected in the simulation. Iteratively, conversion coefficients for each crystal were adjusted until the  $E/p$  ratio in data and simulation were similar. The distribution of the  $E/p$  ratio in data and simulation are compared in Figure 17. The peak of the distribution, at  $E/p \sim 0.7$ , gives the sampling fraction of the ECal, the fraction of the incident particle energy measured in the cluster. The width of the distribution indicates the energy resolution, which is worse than the required  $5\%/\sqrt{E}$  for HPS due to high thresholds. The width in data is greater than that in simulation due to non-uniformity of the calibration of different parts of the ECal.

The A' trigger in HPS is relatively insensitive to the energy of the clusters and this level of performance would be adequate. However, improvements are needed to achieve the expected energy resolution in HPS. The noise and thresholds need to be closer to 10 MeV and a more elaborate calibration technique needs to be employed to suppress the large tails in the  $E/p$  distribution further. In addition, the fraction of working channels needs significant improvement.

### 7.3. Trigger Performance

As described above in Sec. 6, the energy from each crystal is determined slightly differently in the trigger and in the readout. The trigger performance was studied by simulating the trigger for each event and comparing to how the events were actually triggered. To eliminate trigger bias, we use a tag and probe method: to study the trigger performance in one half of the ECal, we select events which triggered the other half and where there

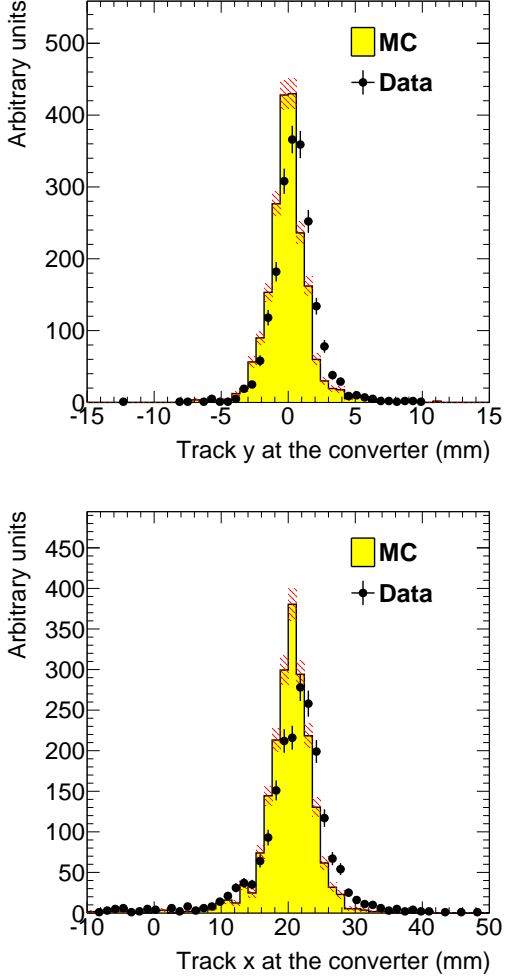


Figure 16: Vertical (top) and horizontal (bottom) extrapolated track position at the converter position taking into account the measured fringe field.

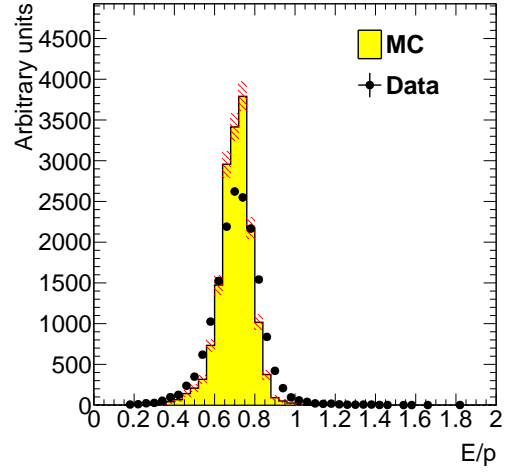


Figure 17: The ECal energy over track momentum ratio ( $E/p$ ) comparing data and simulation for single cluster triggers in the top half of the ECal.

855 was exactly one probe cluster in the ECal half under  
 856 study. We then measure trigger efficiency as the frac-  
 857 tion of tagged events that fired the trigger in the probe  
 858 half as a function of the probe cluster energy, shown  
 859 in Figure 18. The trigger turn-on is slow and reaches  
 860 an uneven plateau at about 700 MeV for two reasons;  
 861 gain variations between different crystals lead to the  
 862 threshold variations and the nonlinearity of the time-  
 863 over-threshold integral means that the effective thresh-  
 864 old is higher for clusters that span multiple crystals. The  
 865 effective trigger threshold is therefore dependent on po-  
 866 sition and energy of the particle as well as cluster multi-  
 867 plicity. For HPS the trigger cluster threshold will be set  
 868 at a lower value.

869 As a cross-check we simulate the FADC trigger path  
 870 by converting from readout hits (with fixed-size win-  
 871 dows integration) to trigger hits (time-over-threshold in-  
 872 tegration). The CTP clustering algorithm and the trigger  
 873 decision from the SSP are simulated before we com-  
 874 pare the trigger decision and trigger time to what was  
 875 reported by the actual trigger. For every event, the trig-  
 876 ger reports the trigger decision as a bit mask (top half,  
 877 bottom half or both) and the time the trigger fired. The  
 878 turn-on from the trigger threshold was measured to be  
 879 1280 in units of ADC counts as expected. The threshold  
 880 was not perfectly sharp because of uncertainties in the  
 881 conversion from readout to trigger hits described above,  
 882 but based on comparisons with simulation we found that  
 883 the trigger worked exactly as specified.

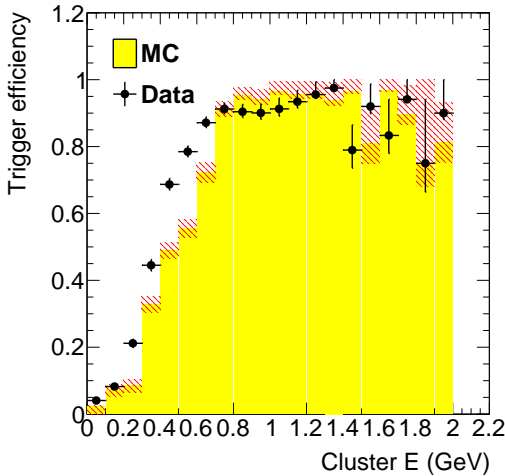


Figure 18: Trigger efficiency in both halves of the ECal for data and simulation as a function of cluster energy.

Converter (% $X_0$ )	<b>1.60</b>	<b>0.45</b>	<b>0.18</b>
EGS5	$1162 \pm 112$	$255 \pm 28$	$94 \pm 17$
Geant4	$2633 \pm 250$	$371 \pm 38$	$114 \pm 18$
Observed	$1064 \pm 2$	$196 \pm 1$	$92 \pm 1$

Table 4: Observed and predicted event rate (in Hz) normalized to 90 nA for three different converter thicknesses. The uncertainty on the prediction includes systematic uncertainties from ECal alignment, background normalization, beam current normalization and limited statistics in the simulation.

#### 7.4. Trigger Rate Comparisons

Trigger rates observed in the HPS Test Run are dominated by  $e^+e^-$  pairs produced in the converter. In simulated events, the rate of triggers depend on the modeling of the pairs' angular distribution and the subsequent multiple Coulomb scattering in the converter. Rates from different converter thicknesses are used to study the varying multiple Coulomb scattering contribution (pair production angular distribution is constant). These rates are compared with those predicted by the standard Geant4 [24] approximation for multiple scattering and the more accurate model used by EGS5 [25]. Restricting to a well calibrated region of the ECal and to clusters with energy above the trigger turn-on, we see agreement with the rates predicted by the EGS5 simulation program after subtracting the “no converter” background , see Table 4. This gives further confidence that the dominant source of background occupancy for HPS, multiple Coulomb scattered beam electrons, is well described.

## 8. Summary and Outlook

The HPS Test Run experiment, using a simplified version of the apparatus planned for the full HPS experiment in a parasitic photon beam, demonstrated the feasibility of the detector technologies proposed for the silicon vertex tracker, electromagnetic calorimeter, and data acquisition systems. Performance from each of these subsystems has been shown to be adequate to conduct the full experiment successfully with some identified improvements. Studies of multiple Coulomb scattering tails of electrons and positrons from photon conversions further backs expectations from simulation, giving credence to estimates of the detector backgrounds expected in electron beam running for HPS.

## 9. Acknowledgements

The authors are grateful for the support from Hall B at JLab and especially the Hall B engineering group for support during installation and decommissioning. They also would like to commend the CEBAF personnel for good beam performance, especially the last few hours of operating CEBAF6. The tremendous support from home institutions and supporting staff also needs praise from the authors.

This work has been supported by the US Department of Energy, the National Science Foundation, French Centre National de la Recherche Scientifique and Italian Istituto Nazionale di Fisica Nucleare. Rouven Essig is supported in part by the Department of Energy Early Career research program DESC0008061 and by a Sloan Foundation Research Fellowship. Authored by Jefferson Science Associates, LLC under U.S. DOE Contract No. DE-AC05-06OR23177.

## References

- [1] B. Holdom, Two U(1)'s and Epsilon Charge Shifts, Phys.Lett. B166 (1986) 196.
- [2] P. Galison, A. Manohar, TWO Z's OR NOT TWO Z's?, Phys.Lett. B136 (1984) 279.
- [3] R. Essig, J. A. Jaros, W. Wester, P. H. Adrian, S. Andreas, et al. (Report of the Community Summer Study 2013 (Snowmass) Intensity Frontier New, Light, Weakly-Coupled Particles subgroup), Dark Sectors and New, Light, Weakly-Coupled Particles, 2013. URL: <http://arxiv.org/abs/arXiv:1311.0029>.
- [4] M. Pospelov, Secluded U(1) below the weak scale, Phys.Rev. D80 (2009) 095002.
- [5] O. Adriani, et al. (PAMELA Collaboration), An anomalous positron abundance in cosmic rays with energies 1.5-100 GeV, Nature 458 (2009) 607–609.

- 952 [6] M. Ackermann, et al. (Fermi LAT Collaboration), Measurement  
 953 of separate cosmic-ray electron and positron spectra with  
 954 the Fermi Large Area Telescope, Phys.Rev.Lett. 108 (2012)  
 955 011103.
- 956 [7] M. Aguilar, et al. (AMS Collaboration), First Result from the  
 957 Alpha Magnetic Spectrometer on the International Space Station:  
 958 Precision Measurement of the Positron Fraction in Primary Cosmic  
 959 Rays of 0.5350 GeV, Phys.Rev.Lett. 110 (2013) 141102.
- 960 [8] N. Arkani-Hamed, D. P. Finkbeiner, T. R. Slatyer, N. Weiner, A  
 961 Theory of Dark Matter, Phys.Rev. D79 (2009) 015014.
- 962 [9] M. Pospelov, A. Ritz, Astrophysical Signatures of Secluded  
 963 Dark Matter, Phys.Lett. B671 (2009) 391–397.
- 964 [10] J. D. Bjorken, R. Essig, P. Schuster, N. Toro, New Fixed-Target  
 965 Experiments to Search for Dark Gauge Forces, Phys.Rev. D80  
 966 (2009) 075018.
- 967 [11] A. Grillo, et al. (HPS Collaboration), Heavy Photon Search  
 968 Proposal, 2010. URL: [https://confluence.slac.stanford.edu/download/attachments/86676777/HPSProposal-FINAL\\_Rev2.pdf](https://confluence.slac.stanford.edu/download/attachments/86676777/HPSProposal-FINAL_Rev2.pdf).
- 969 [12] A. Sandorfi, et al., 2012. URL: [http://www.jlab.org/exp\\_prog/proposals/06/PR06-101.pdf](http://www.jlab.org/exp_prog/proposals/06/PR06-101.pdf).
- 970 [13] F.-X. Girod, M. Garon (CLAS), Inner calorimeter in clas/dvcs  
 971 experiment, CLAS-Note 2005-001 (2005).
- 972 [14] R. Niyazov, S. Stepanyan (CLAS), Clas/dvcs inner calorimeter  
 973 calibration, CLAS-Note 2005-021 (2005).
- 974 [15] F.-X. Girod (Universite de Strasbourg), 2006. URL: <http://www.jlab.org/Hall-B/general/thesis/fxggirod.pdf>.
- 975 [16] I. Rashevskaya, S. Bettarini, G. Rizzo, L. Bosisio, S. Dittongo,  
 976 et al., Radiation damage of silicon structures with electrons of  
 977 900-MeV, Nucl. Instrum. Meth. A485 (2002) 126–132.
- 978 [17] D. S. Denisov, S. Soldner-Rembold, D0 Run IIB Silicon Detec-  
 979 tor Upgrade: Technical Design Report (2001).
- 980 [18] M. French, L. Jones, Q. Morrissey, A. Neviani, R. Turchetta,  
 981 et al., Design and results from the APV25, a deep sub-micron  
 982 CMOS front-end chip for the CMS tracker, Nucl.Instrum.Meth.  
 983 A466 (2001) 359–365.
- 984 [19] M. Friedl, C. Irmler, M. Pernicka, Readout of silicon strip detec-  
 985 tors with position and timing information, Nucl.Instrum.Meth.  
 986 A598 (2009) 82–83.
- 987 [20] H. Dong, et al., Integrated tests of a high speed VXS switch  
 988 card and 250 MSPS flash ADCs, 2007. doi:10.1109/NSSMIC.  
 989 2007.4436457.
- 990 [21] R. Larsen, Emerging New Electronics Standards for Physics,  
 991 Conf.Proc. C110904 (2011) 1981–1985.
- 992 [22] L. Jones, APV25-S1: User guide version 2.2, RAL Microelec-  
 993 tronics Design Group, 2011.
- 994 [23] M. Friedl, C. Irmler, M. Pernicka, Obtaining exact time infor-  
 995 mation of hits in silicon strip sensors read out by the APV25  
 996 front-end chip, Nucl. Instrum. Meth. A572 (2007) 385 – 387.
- 997 [24] S. A. et al., GEANT4 - a simulation toolkit, Nucl.Instrum.Meth.  
 998 A506 (2003) 250 – 303.
- 999 [25] H. Hirayama, Y. Namito, A. Bielajew, S. Wilderman, W. Nelson,  
 1000 The EGS5 Code System, 2005.
- 1001
- 1002
- 1003
- 1004
- 1005